Dynamical localization of ultracold sodium atoms

C. F. Bharucha,* J. C. Robinson,† F. L. Moore,‡ Bala Sundaram,§ Qian Niu, and M. G. Raizen
Department of Physics, The University of Texas at Austin, Austin, Texas 78712-1081
(Received 10 August 1998; revised manuscript received 21 May 1999)

We report a study of atomic motion in time-dependent optical potentials. We measure momentum transfer in parameter regimes for which the classical dynamics are chaotic, and observe the quantum suppression of chaos by dynamical localization. The high degree of control over the experimental parameters enables detailed comparisons with theoretical predictions, and opens new avenues for investigating quantum chaos. [S1063-651X(99)12609-6]

PACS number(s): 05.45.−a

I. INTRODUCTION

The past few years have seen a resurgence in the use of classical mechanics in the description of strongly perturbed and strongly coupled quantum systems in atomic physics [1,2], where the traditional perturbative treatment of the Schrödinger equation breaks down. In particular, recent advances in classical nonlinear dynamics and chaos have had important applications in the description of the photoabsorption spectrum of Rydberg atoms in strong magnetic fields [3], the microwave ionization of highly excited hydrogen atoms [4], and the excitation of doubly excited states of helium atoms [5]. These examples, together with recent work on mesoscopic systems [6], explore classical-quantum correspondence in situations that exhibits chaos in the classical limit, an area of study referred to as ''quantum chaos'' [7].

Parallel developments in laser cooling and trapping techniques have led in recent years to spectacular advances in the manipulation and control of atomic motion [8]. At the ultracold temperatures that are now attainable, the wave nature of atoms becomes important. These advances have led to the development of the new field of atom optics [9]. Until recently, the primary focus in atom optics has been the development of optical elements such as atomic mirrors, beam splitters, and lenses for atomic de Broglie waves. Our work has emphasized the regime of time-dependent potentials, and hence of dynamics, in atom optics. In particular, we study momentum distributions of ultracold atoms exposed to time-dependent, one-dimensional, optical dipole forces that are typically highly nonlinear. Thus the classical motion can become chaotic. As dissipation may be made negligibly small in this system, quantum-mechanical effects can become important. Our work has established that these features together make atom optics a simple and controlled setting for the experimental study of quantum chaos [10].

A particular focus for our discussions is the phenomenon of dynamical localization [11], which is an important mechanism for the quantum suppression of classical chaotic dynamics. Though initially predicted in a simple time-dependent paradigm system called the δ-kicked rotor, it has been since shown to be a universal effect in a class of dynamical systems [12]. In brief, the chaotic evolution of a classical ensemble of particles results in a diffusive growth of energy. Under certain conditions, however, the quantum dynamics follows this growth only for a limited time, called the break time, after which it saturates. At this point, the particles also assume a distinctive exponential probability distribution in momentum (in the one-dimensional case). This numerically observed effect has also been shown to be closely related to Anderson localization, which describes a metal-insulator transition at low temperatures [13,14].

This paper describes our work on the interaction of an ensemble of cold atoms with two particular time-dependent optical potentials. Both optical potentials were created by the interaction of the atoms with a standing wave of light. The first interaction was a direct realization of the paradigm kicked system. By contrast, the second was a continuous-time interaction, which nonetheless exhibited the same phenomenon of dynamical localization. Together, these experiments and the accompanying analysis have provided a controlled context for the study of dynamical localization and quantum chaos [10].

This paper starts with this introduction, and continues in Sec. II with a background description of the interaction between the cooled atoms and the standing wave in our experiment, and of the simulations used to model the interaction. Section III proceeds with a detailed description of our experimental realization of this system, including the method by which we cooled the atomic sample to create the initial conditions for the interaction, the system for making the standing wave that imposed the interaction potential, and the techniques for measuring the final momentum distribution of the atomic sample after the interaction. Section IV presents the experiments that realized the kicked rotor, and Sec. V concerns the experiments in which the atomic sample was exposed to a continuous phase-modulated standing wave. These two sections each present a classical analysis of the system, and describe how the quantum predictions differ from this analysis. In addition, Sec. IV presents our observations and analyses of quantum resonances. The work is summarized in Sec. VI.

*Present address: Conley, Rose and Tayon, P.C., 816 Congress Ave., Suite 320, Austin, TX 78701.
†Present address: KLA-Tencor, 1701 Directors Blvd., Suite 1000, Austin, TX 78744.
‡Present address: NOAA/CMDL, NO_2 and Halocompounds Division, 325 Broadway, Boulder, CO 80303.
§Present address: Department of Mathematics, CSI-CUNY, Staten Island, NY 10314.

II. BACKGROUND: A TWO-LEVEL ATOM IN A STANDING-WAVE POTENTIAL

A. Physical model

Consider a two-level atom of transition frequency ω_o interacting with a standing wave of near-resonant light. If the standing wave is composed of two counterpropagating linearly polarized beams, each with field amplitude $E_o\hat{y}$ and wave number $k_L=2\pi/\lambda_L=\omega_L/c$, then the atom is subjected to an electric field $\vec{E}(x,t)=2E_o\hat{y}\cos(k_Lx)\cos(\omega_Lt)$, where x and p are the center-of-mass position and momentum of the atom.

If the laser light is tuned far from atomic resonance, it can be shown [15,16] that the center-of-mass motion of the atom in the standing-wave field can be described by a one-dimensional Schrödinger equation for a point particle, with a Hamiltonian given by

$$H(x,p,t)=\frac{p^2}{2M}+V_o\cos 2k_Lx. \tag{1}$$

Here M represents the mass of the atom. The potential has a period of one-half the optical wavelength, and an amplitude V_o that is proportional to the intensity of the standing wave and inversely proportional to its detuning, $V_o=\frac{2}{3}\hbar(\Gamma/2)^2I/\delta_LI_{\rm sat}$, where Γ is the linewidth of the transition and I is the intensity (irradiance) of each of the beams in the standing wave, the detuning is given by $\delta_L\equiv\omega_L-\omega_o$, and $I_{\rm sat}\equiv\pi\hbar\omega_o\Gamma/3\lambda_L^2$ is the saturation intensity for the transition. For the D_2 transition in sodium atoms, the saturation intensity has a value of $I_{\rm sat}=6$ mW/cm^2. In the case where the two constituent beams of the standing wave are not perfectly matched, I represents the geometric mean of their two intensities.

The Hamiltonian in Eq. (1) is readily recognized as the simple pendulum or rotor, except that the conjugate variables are now position and momentum rather than the usual angle and angular momentum. This distinction becomes relevant for some quantum applications, as described in Sec. IV D and in Ref. [17]. The pendulum equation is an important starting point in the study of nonlinear dynamics, and the optical system represented by Eq. (1) is a valuable realization of this one-dimensional paradigm.

B. Time-dependent interaction

Equation (1) illustrated the realization of a system in which the atomic motion is analogous to the behavior of a pendulum. We can exploit the control available in the experiment on the optical standing wave to achieve more interesting systems. By adding a time dependence to the laser intensity, we can vary the amplitude of the potential as a function of time. Also, by differentially shifting the optical phases (or frequencies) of the beams that compose the standing wave, we can vary its position (or velocity) as a function of time. With these considerations, we see that the electric field of the standing wave takes the form $\vec{E}(x,t)=\hat{y}E_oF_1(t)\cos\{k_L[x-F_2(t)]\}\cos(\omega_Lt)$, where $F_1(t)$ and $F_2(t)$ represent the controls applied to the amplitude and phase, respectively, of the optical standing wave. The time scales for these controls ranged between $\sim$25 ns (the response time of our optical modulators) and milliseconds (the duration of the experiments). The amplitude and phase modulations were therefore slow compared to the parameters ω_o and δ_L relevant to the derivation of Eq. (1), so they change that equation by simply modifying the amplitude and phase of the sinusoidal potential. The generic time-dependent potential thus has the form

$$H(x,p,t)=\frac{p^2}{2M}+V_oF_{\rm amp}(t)\cos[2k_Lx-F_{\rm ph}(t)]. \tag{2}$$

The parametric dependence of this system becomes clear on switching to dimensionless variables of time ($\tau=t/t_u$), displacement along the standing wave ($\phi=2k_Lx$), and the atomic momentum ($\rho=p\,2k_Lt_u/M$). In these scalings, the quantity t_u is an appropriate time scale chosen with regard to the time dependence of the interaction. These transformations, together with an energy scale defined by $\mathcal{H}(\phi,\rho,\tau)=H(x,p,t)8\omega_rt_u^2/\hbar$, lead to the dimensionless Hamiltonian

$$\mathcal{H}(\phi,\rho,\tau)=\frac{\rho^2}{2}+kf_{\rm amp}(\tau)\cos[\phi-f_{\rm ph}(\tau)]. \tag{3}$$

The scaled potential amplitude here is $k\equiv V_o8\omega_rt_u^2/\hbar$, and $f_{\rm amp}$ and $f_{\rm ph}$ represent the amplitude and phase controls imposed on the optical standing wave. The recoil-shift frequency $\omega_r=\hbar k_L^2/2M$ is a characteristic of the atomic transition. In these transformed variables, the Schrödinger equation in the position representation becomes

$$i\bar{\hbar}\frac{\partial}{\partial\tau}\Psi(\phi,\tau)=\left[-\frac{\bar{\hbar}^2}{2}\frac{\partial^2}{\partial\phi^2}+kf_{\rm amp}(\tau)\times\cos[\phi-f_{\rm ph}(\tau)]\right]\Psi(\phi,\tau). \tag{4}$$

The dimensionless quantization scale $\bar{\hbar}$ results from the commutation relation between momentum and position $[\phi,\rho]=i\bar{\hbar}$, and is given by $\bar{\hbar}\equiv8\omega_rt_u$.

As with the classical analyses of this system, the quantum analysis is similar to that of a pendulum. In the quantum picture, however, it is important to note a distinction between our system and a pendulum. As noted earlier, the conjugate variables for this system are position and momentum rather than angle and angular momentum. The distinction is one of more than nomenclature. The basis states for a pendulum have the spatial boundary condition $\Psi_l(\phi+2\pi)=\Psi_l(\phi)$. In contrast, the basis states for an atom in the optical potential have the more general Bloch condition $\Psi_l(\phi+2\pi)=e^{i2\pi\nu}\Psi_l(\phi)$, where ν indicates the quasimomentum of the basis state. A quantum description of the atom's dynamics must therefore consider the general case where the eigenstates have different values of quasimomentum.

Another general note on this transformation concerns the measure of the atomic momentum. Since an atom interacts with a near-resonant standing wave, its momentum can be changed by stimulated scattering of photons in the two counterpropagating beams. If a photon is scattered from one of these beams back into the same beam, the result is no net change in the atom's momentum. But if the atom scatters a

photon from one of the beams into the other, the net change in its momentum is two photon recoils. The atom can thus exchange momentum with the standing wave only in units of $2\hbar k_L = 2$ recoils $= 6$ cm/s$\times M$. This quantization of momentum exchange can also be seen by considering the effect of the optical potential on an atomic plane wave with momentum p_o. Because of the optical potential's spatial periodicity, it couples the plane wave only to an evenly spaced ''ladder'' of plane waves with momenta $p_o \pm 2n\hbar k_L$. Thus the exchange of momentum is restricted to multiples of $2\hbar k_L$.

Since the atomic momentum is naturally measured in this unit of momentum transfer, we use the quantity $p/2\hbar k_L$ when describing measured momenta in this paper. In the transformed, dimensionless units, this quantity is

$$\frac{p}{2\hbar k_L} = \frac{\rho}{\bar{\kappa}}. \tag{5}$$

For a sample of atoms initially confined to a momentum distribution narrower than one recoil, the discreteness of the momentum transfer would result in a final momentum distribution characterized by evenly spaced peaks, with the peaks located on the ladder of coupled momentum states. In our experiments, the initial momentum distributions were significantly wider than two recoils ($\sigma_{po}/2\hbar k_L \sim 2.3$), so the observed final momenta had smooth distributions rather than discrete structures.

C. Simulations

A careful characterization of the experimental conditions is necessary for a detailed comparison with theoretical predictions, both analytical and numerical. This motivation leads naturally to the question of what initial state should be used in the quantum simulations to model the initial sample of atoms used in the experiment. The choice is motivated by several factors.

Our initial atomic sample was prepared in a magneto-optic trap that cooled the sodium atoms to a distribution that was Gaussian in momentum and position. Although the wave functions for individual atoms in the sample were not known, the *ensemble* of atoms had a well-characterized distribution. As described below in Sec. III, the rms momentum width of the distribution was roughly $4.6\hbar k_L$ (or, in scaled units, $\sigma_\rho \sim 2.3$), and its spatial width was large in comparison to the period of the standing wave. It should be noted that the atoms in the atomic sample are essentially noninteracting, and so the observed effects are essentially single-particle effects. Thus a wave packet evolving according to the Schrödinger equation would be a natural choice to describe the behavior of the atomic sample. In our choice of the initial wave packet, we considered that the initial sample of atoms was directly measured to have a Gaussian distribution in momentum. The spatial and momentum widths of the distribution are unrelated, precluding the use of a single minimum-uncertainty wave packet, although a superposition of minimum-uncertainty packets [18] can be used. Also, as illustrated by the analysis of the quantum resonances in Sec. IV D, the calculation can be performed by time-evolving an ensemble of initial plane-wave states weighted by the Gaussian distribution and summing the final probability distributions.

In our space-time integration of the Schrödinger equation, the initial state is a ''squeezed'' Gaussian wave packet

$$\Phi(\phi) = (2\pi\sigma_\phi^2)^{1/4} \exp[-A(\phi-\overline{\phi})^2 + i\overline{\rho}(\phi-\overline{\phi})/\bar{\kappa}], \tag{6}$$

where $A \equiv (1 - 2i\sigma_{\phi\rho}/\bar{\kappa})/4\sigma_\phi^2$. This wave packet has centroid (mean) values of position and momentum given by $\overline{\phi}$ and $\overline{\rho}$. Its variances σ_ϕ^2, σ_ρ^2, and $\sigma_{\phi\rho} \equiv \langle (\phi-\overline{\phi})(\rho-\overline{\rho}) + (\rho-\overline{\rho})(\phi-\overline{\phi})\rangle/2$ are related by the uncertainty condition $\sigma_\phi^2\sigma_\rho^2 = (\bar{\kappa}/2)^2 + \sigma_{\phi\rho}^2$. With this wave packet, the initial widths in ϕ and ρ may be independently specified by adjusting the anticommutator $\sigma_{\phi\rho}$ to maintain the uncertainty condition. In our simulations we chose the momentum width σ_ρ to match the measured initial value in the experiment, and set the spatial width σ_ϕ to be large with respect to a period of the standing wave (2π in these units). Although it is clear that Eq. (6) is a very special initial condition with special coherence properties, simulations using this wave packet agree well with the observations from our experiments to observe dynamical localization. This agreement will be seen in our analyses of quantum resonances (Sec. IV D). As will be shown by our simulations of the modulated standing-wave system (Sec. V C), there is also very close agreement between our squeezed-wave-packet analysis and results obtained using plane-wave and coherent-state superpositions. The agreement among these calculations and with the experimental observations indicates that the dynamics of localization is not sensitive to the form of the initial condition. In some sense, this is not surprising. The classical chaotic dynamics leads to a randomization of phase in the quantum evolution (readily seen from an analogy with Anderson localization [13]). This randomization destroys any special coherences present in the initial condition; thus any coherence in the final distribution is a result purely of the dynamics. A detailed analysis of the more complicated issue of mixed versus pure state evolution in the context of these experiments will be presented elsewhere [19].

III. EXPERIMENTAL METHOD

The experimental study of momentum transfer in time-dependent interactions consists of three important components: the initial conditions, the interaction potential, and the measurement of atomic momentum. The initial distribution ideally should be narrow in position and momentum, and should be sufficiently dilute so that atom-atom interactions can be neglected. The time-dependent potential should be one dimensional, for simplicity, with full control over the amplitude and phase. In addition, noise and dissipation must be minimized to enable the study of quantum effects. Finally, the measurement of final momenta after the interaction should be highly sensitive and accurate. It is possible to realize all these conditions using the techniques of laser cooling and trapping. This section describes the apparatus and

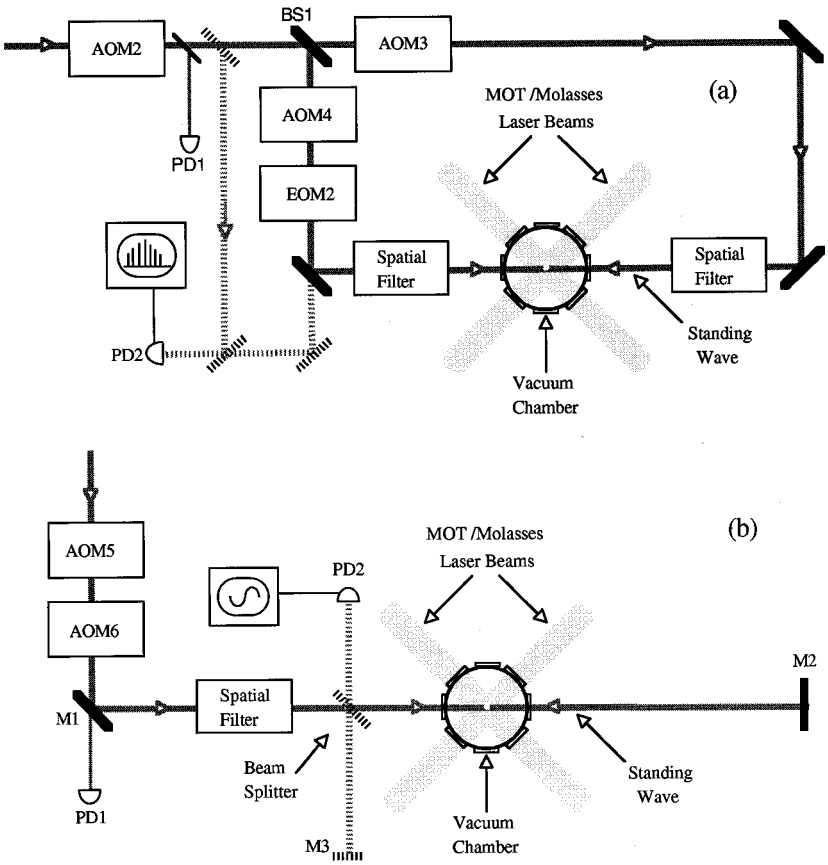

FIG. 1. Beam configurations for the experiments. Laser beams illuminate the atoms in the vacuum chamber in a standard σ^+-σ^- configuration, to provide cooling and trapping (molasses and MOT). The standing-wave beam is the source of the interaction potential for the trapped and cooled sodium atoms. For the experiments of Sec. V, the standing wave was constructed of two counterpropagating beams with separate frequency shifts as depicted in part (a) of this figure. A differential shifting of the two beams provided the required control on the velocity of the standing wave. For the experiments of Sec. IV, the layout in (b) was used to provide the required control over the standing-wave amplitude while holding its position fixed.

techniques used in our experiments. Further details on the realization of these experiments can be found in Ref. [20].

A. Initial conditions

Our initial conditions were a sample of ultracold sodium atoms that were trapped and laser-cooled in a magneto-optic trap (MOT) [8,21]. The atoms were contained in a quartz ultrahigh-vacuum cell at room temperature. The trap was formed with three pairs of counterpropagating, circularly polarized laser beams with diameters of roughly 2 cm. These beams intersected in the center of the glass cell, together with a magnetic field gradient provided by current-carrying wires arranged in an anti-Helmholtz configuration. This σ^+-σ^- configuration is standard, and is used in many laboratories. A dye laser supplied the MOT beams. The laser was locked by saturated-absorption FM spectroscopy to a frequency 65 MHz to the blue of the $(3S_{1/2},F=2) \rightarrow (3P_{3/2},F=3)$ sodium transition at $\lambda_L = 2\pi/k_L = 589$ nm.

Using this scheme, we trapped approximately 10^5 atoms into a cloud that had a Gaussian distribution in position with a rms width of $\sigma_{xo} = 0.12$–0.17 mm. The sample of atoms had a Gaussian distribution in momentum, with a spread of $\sigma_{po} = 4.6$-$6\hbar k_L$, corresponding to a temperature of 25–45 μK. (The accuracy of these measurements was better than the variation in MOT size and momentum.) This confined, cold distribution defined the initial conditions of the sample of atoms before they were exposed to the interaction potential.

B. Interaction potential

A second dye laser provided the optical standing wave that formed the interaction potential. This laser was typically tuned 5−10 GHz from resonance. Different beam configurations were used in the experiments described here, with acousto-optic and electro-optic modulators controlling the time-dependent amplitude and phase.

Figure 1(a) shows the configuration for the modulated standing-wave experiment of Sec. V. An acousto-optic modulator (AOM2 in the figure) turned the interaction potential on and off with a 10−90 % switching time of 25 ns. The beam's power was monitored on a photodiode (PD1). The light was then split into a pair of spatially filtered beams that overlapped to form a standing wave intersecting the trapped atoms in the vacuum cell. These two beams were considerably wider than the distribution of atoms, with typical waists of 1.9 mm. An electro-optic modulator (EOM2) shifted the phase of one of the beams, and hence the position of the standing wave along its axis. The magnitude of this shift was determined by inserting the Mach-Zehnder interferometer indicated by the dashed lines in Fig. 1(a) and analyzing the PM sidebands in the heterodyne signal on photodiode PD2. The velocity of the standing wave in the lab frame also could be varied by introducing a differential frequency shift between the two beams with two more acousto-optic modulators (AOM3 and AOM4). These elements provided the control, indicated by $F_{\rm ph}(t)$ in Eq. (2), over the position—or phase—of the standing-wave potential as a function of time.

To modulate the phase of the potential, we varied the phase of one of the two laser beams that make the standing wave. The electro-optic modulator EOM2 in Fig. 1(a) provided this control. By applying an oscillating drive $V_{\rm EO} \sin \omega_m t$ we modulated the phase of the beam with an amplitude $\pi V_{\rm EO}/V_\pi$, and gave the phase of the standing wave a time dependence $\lambda \sin \omega_m t$, with $\lambda \equiv 2k_L \Delta L = \frac{1}{2}\pi V_{\rm EO}/V_\pi$.

To calibrate the modulation index λ with the voltage applied across the EO, we performed an optical heterodyne measurement, as shown by the dotted lines in Fig. 1(a). During the calibration, AOM4 imparted a 40-MHz frequency offset in the beam that passed through it, and EOM2 added a phase modulation of $\lambda \sin \omega_m t$. The signal from photodiode PD2 was observed on a spectrum analyzer. A beat note at 40 MHz was seen, along with frequency sidebands at plus and minus integer multiples of $\omega_m/2\pi = 1.3$ MHz away from 40 MHz. These sidebands had amplitudes given by the Bessel functions of the modulation index: the amplitude of the nth-order sideband scaled with $J_n(\lambda)$. By varying the amplitude V_{EO} of the rf drive to EOM2, the frequency sidebands go to zero as the corresponding Bessel functions go through a zero. By correlating the applied voltages V_{EO} that led to zeros in the sidebands with the corresponding modulation indices, a calibration between voltage and modulation index was acquired. Since the modulation index was substantially linear in the applied voltage, interpolation between the calibrated points provided a measure of the values of λ used in the experiments with an accuracy of better than 1%.

For the kicked rotor experiments described in Sec. IV, a simpler configuration was used. In these experiments, the position of the standing wave was fixed, and its amplitude was varied to produce the time-dependent interactions. The interaction Hamiltonian thus had the form of Eq. (2), with $F_{\mathrm{ph}}(t)$ fixed and the time dependence imposed through $F_{\mathrm{amp}}(t)$. The configuration for these experiments is depicted in Fig. 1(b). The standing wave was formed here by training the beam directly onto the atomic sample and retroreflecting the beam with mirror $M2$, effectively doubling the available power while providing a fixed node in the standing wave at the surface of the retroreflecting mirror. The initial element (AOM5) was an acousto-optic modulator that could diffract 80% of the optical power into the first-order spot. This fast modulator, with a 10% to 90% rise time of 25 ns, provided the amplitude modulation of the interaction beam. The next acousto-optic modulator (AOM6) provided additional amplitude control for experiments in which we carried out preliminary studies of the effects of amplitude noise on the dynamics. Photodiode PD1 monitored the temporal pulse profiles during the experiments. These profiles were digitized and stored for later analysis. To measure the phase stability of the standing wave, a Michelson interferometer was constructed by inserting a beam splitter as shown by the dashed marks in Fig. 1(b). This measurement indicated that the standing-wave phase at the atomic sample was stable to within a few percent of a period for times up to 100 μs.

To what extent is Eq. (1) a good representation of a sodium atom exposed to the optical standing wave in these experiments? The assumptions used in the derivation of this equation are appropriate for these systems. The two-level atom model and the rotating-wave approximation are well justified for the optical-frequency transition. Also, an adiabatic elimination of the excited-state amplitude is appropriate for detunings δ_L that are large in comparison to the linewidth Γ and the recoil-shift frequency ω_r, which are both characteristics of the atomic transition. Specifically, for the sodium D_2 transition $\Gamma/2\pi = 10$ MHz and $\omega_r/2\pi = 25$ kHz. Our experimental detunings of several GHz clearly satisfied these conditions. The large detuning also led to a small probability of spontaneous emission during the experiments. It is also important to note that for the sodium D_2 transition in linearly polarized light, the light shift was the same for all the m_F sublevels. As a consequence, it was not necessary to prepare the atoms in specific m_F sublevels for them to experience the same optical potentials in the experiment.

The one-dimensional nature of Eq. (2) comes from the assumption that the laser beams have spatially uniform transverse profiles. In these experiments the width of the atomic sample ($\sigma_{xo} \sim 0.15$ mm rms) during the illumination by the standing wave was small compared to the width of the laser profile (which had a $1/e$ field waist of $w_o \sim 1.9$ mm), so the transverse variations in the potential were indeed small. The optical potential also had an uninterrupted periodic structure over the entire spatial extent of the atomic sample. Since the standing wave had a coherence length (tens of meters) that was large compared to the difference in pathlength taken by its two component beams (~ 1 m), the periodicity of the potential was coherent over the entire region of the atomic sample. Unlike the periodic potentials in condensed matter systems, this realization is thus effectively free from imperfections in the lattice periodicity as well as from dissipation mechanisms such as phonon scattering.

C. Measurement of the atomic momentum

Our original vision of these experiments involved an atomic beam whose transverse momentum distribution would be affected by interactions with the standing wave. The interactions could then be characterized by observing the transverse spatial distribution of the atomic beam some distance after it had passed through the standing wave. A very important simplification in the design of these experiments was the formulation of an alternative scheme for measuring the momentum transferred to the atoms from the standing wave.

The method we developed to make this measurement greatly simplified the data collection and obviated the need for an atomic beam altogether. The method is illustrated in Fig. 2. Panel (a) of this figure shows the initial condition of a spatially confined and cooled atomic sample created by the MOT. After being exposed to the interaction potential in our experiments, as shown in panel (b), the atoms had a new momentum distribution, but the duration of the interactions was short enough that their spatial distribution remained essentially unchanged. They were then allowed to drift in the dark for a controlled duration t_{drift} of a few milliseconds, as illustrated in panel (c). During this time, the atoms underwent ballistic motion and their momentum distribution resulted in a widened spatial distribution. We then measured the spatial distribution of the atoms. Their motion was frozen by turning on the optical trapping beams in zero magnetic field to form optical molasses [8], as shown in panel (d). Under these conditions of ''freezing molasses'' the atoms' motion is rapidly damped, and for short times (tens of ms) their motion is negligible in comparison to the dimensions of the sample. A charge-coupled-device (CCD) camera was used to image the fluorescence of the atoms in this molasses. The resulting image recorded the new spatial distribution of the atoms, and since we knew the time of flight t_{drift} we were able to derive the atomic momentum distribution from the

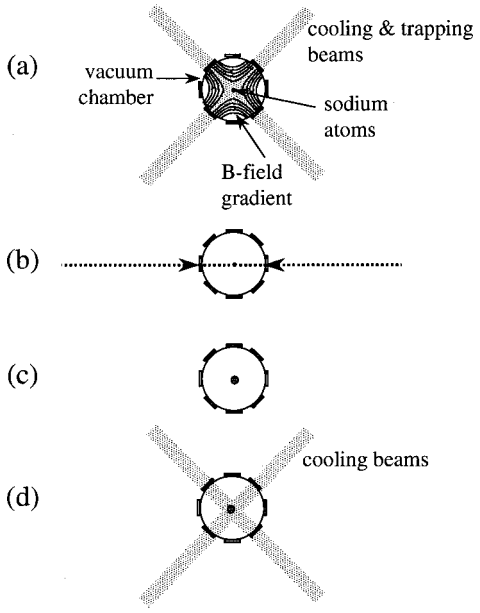

FIG. 2. Procedure for measuring the atomic momentum distribution. After the reproducible initial preparation of a spatially confined and cooled sample of atoms (a), the atoms were exposed to an interaction potential (b). To measure the effect of the interaction on the sample's momentum distribution, the atomic sample was then allowed to expand freely for a controlled time t_{drift} (c) that was long in comparison to the interaction time from step (b). After the free expansion, the final spatial distribution was frozen in optical molasses (d) and imaged. The final momentum distribution was then determined by deconvolving the initial spatial distribution from the final spatial distribution, and by considering the time t_{drift} over which the expansion occurred.

spatial distribution. The entire sequence of the experiment was computer controlled.

IV. KICKED ROTOR

The classical δ-kicked rotor, or the equivalent standard mapping, is a textbook paradigm for Hamiltonian chaos [22,7]. The Hamiltonian for the problem is given by

$$\mathcal{H}(\phi,\rho,\tau)=\frac{\rho^2}{2}+K\cos\phi\sum_{n=-\infty}^{\infty}\delta(\tau-n). \tag{7}$$

The evolution consists of a series of impulses, spaced equally in time, whose strengths are governed by the free motion between successive kicks. The magnitude K of the impulse is called the stochasticity parameter; it is this quantity that controls the dynamics for the system.

Using a Fourier expansion, Eq. (7) can be rewritten as

$$\mathcal{H}=\frac{\rho^2}{2}+\sum_{m=-\infty}^{\infty}K\cos(\phi-m2\pi\tau). \tag{8}$$

The potential here is a series of pendulumlike terms, each of which has the form of the potential in Eq. (1). These terms, however, are displaced in velocity by $d\phi/d\tau=2m\pi$. For small values of K, the phase portrait of this system is similar to that of the simple pendulum, but it is periodic along the momentum axis. Instead of having one island of closed librational orbits, it has an infinite number of such islands. Each of these *nonlinear resonances* corresponds to one of the pendulumlike terms in Eq. (8). According to the stationary-phase condition, the phase space is described by nonlinear resonances spaced regularly in momentum at $d\phi/d\tau=\rho_m\equiv 2m\pi$. The width of each resonance depends on the amplitude of the corresponding potential term. In the δ-kicked rotor of Eq. (8), these amplitudes all have the uniform value K. For sufficiently large values of K, neighboring resonances ''overlap'' with each other. That is, particles starting at points in phase space between the resonances will exhibit chaotic motion. The quantum version of this problem has also played an important role in the field of quantum chaos, and a wide range of effects has been predicted [23].

In our realization, we have the cosine potential of the standing wave multiplied by a train of pulses with finite amplitude and pulse width. This system was analyzed previously in the context of molecular rotation excitation [24]. To achieve a system of the form in Eq. (7), we fixed the phase of our standing wave but turned its amplitude on and off in a series of N short pulses with period T. The optical arrangement was described in Sec. III [Fig. 1(b)]. The result was an interaction that can be described by the Hamiltonian of Eq. (2) with $F_{\mathrm{amp}}=\Sigma_{n=1}^{N}F(t-nT)$ and $F_{\mathrm{ph}}=0$:

$$H=\frac{p^2}{2M}+V_o\cos(2k_Lx)\sum_{n=1}^{N}F(t-nT). \tag{9}$$

Here the function $F(t)$ is a narrow pulse in time centered at $t=0$ that modulates the intensity of the standing wave. The sum in this equation represents the periodic pulsing of the standing wave: its amplitude V_o is multiplied by a value in the range $0\leqslant F(t)\leqslant 1$.

The fast acousto-optic modulator [AOM5 in Fig. 1(a)] provided the amplitude modulation of the standing wave to form the pulse train $\Sigma F(t)$. This modulator had a 10–90 % rise and fall time of 25 ns. The computer that controlled the experiment downloaded the desired number of pulses and pulse period to a programmable arbitrary wave form generator, which in turn triggered the fast pulse generator. The programmed profile had a constant amplitude, but because of signal limitations in the pulse generator and in AOM5, each pulse had a rounded profile. The consequences of this rounding are discussed below.

With the scaling introduced in Sec. II and the unit of time taken to be T, the period of our pulse train, the Hamiltonian for this system becomes

$$\mathcal{H}=\frac{\rho^2}{2}+K\cos\phi\sum_{n=1}^{N}f(\tau-n). \tag{10}$$

The train of δ functions in Eq. (7) has been replaced here by a series of normalized pulses $f(\tau)=F(\tau T)/\int_{-\infty}^{\infty}F(\tau T)d\tau$. The scaled variable $\tau=t/T$ measures time in units of the pulse period. As described earlier, $\phi=2k_Lx$ is a measure of an atom's displacement along the standing-wave axis, and $\rho=p\,2k_LT/M$ is the dimensionless momentum.

In addition to the temporal profile of the pulses, the experimental parameters that determine the classical evolution of this system are contained in the stochasticity parameter K,

while the quantum evolution depends additionally on the parameter $\bar{k}$. In terms of the physical parameters of Eq. (9), these two dimensionless quantities are

$$K \equiv 8 V_o \alpha T t_p \omega_r / \hbar, \quad \bar{k} = 8 \omega_r T. \tag{11}$$

Here t_p is the full width at half maximum (FWHM) duration of each pulse, and $\alpha \equiv \int_{-\infty}^{\infty} F(t) dt / t_p$ is a shape factor that characterizes the integrated power for a particular pulse profile: it is the ratio of the energy in a single pulse to the energy of a square pulse with the same amplitude and duration. For a train of square pulses, $\alpha = 1$, while for Gaussian pulses, $\alpha = (\pi / 4 \ln 2)^{1/2} = 1.06$. These two cases provide effective bounds for the experimentally realized pulses. As discussed in the following analysis, the exact shape of the pulses does not significantly affect the experimental results if the pulses are sufficiently narrow in time.

A. Classical analysis

The classical equations of motion for the ideal δ-kicked rotor can be integrated over a single impulse, resulting in the Chirikov-Taylor map or ''standard map'' [22,25]. Calculations with this map show chaotic diffusion for values of K greater than ~ 1 [26]. Extensive theoretical and numerical studies have been carried out on the δ-kicked rotor [23]. These studies, however, have typically considered the ideal limit of δ-function pulses. It is important to consider what effects are introduced by the finite width and amplitude of our experimental pulses.

To assess the effects of a finite pulse-width, consider the case where the pulse profile $f(\tau)$ is Gaussian with an rms width τ_{rms}. The potential from Eq. (10) can be expanded in a discrete Fourier series:

$$\mathcal{H} = \frac{\rho^2}{2} + \sum_{m=-\infty}^{\infty} K_m \cos(\phi - 2 m \pi \tau), \tag{12}$$

with

$$K_m \equiv K \exp[-\tfrac{1}{2}(2 m \pi \tau_{\mathrm{rms}})^2]. \tag{13}$$

The nonlinear resonances are located at $\rho_m = 2 m \pi$. This expansion is similar to the resonance structure of the δ-kicked rotor described above [Eq. (8)]. In Eq. (12), however, the widths of successive resonances decrease because of the exponential term in the coefficients K_m. Thus the phase portrait of this system is not periodic along the momentum axis [as was the case for the system of Eq. (8)]. It does, of course, retain the spatial periodicity imposed by the periodicity of the standing wave potential.

Since the coefficient K_m is the amplitude of a nonlinear resonance centered at a velocity of $d\phi/d\tau = 2 m \pi$, it is an effective stochasticity parameter for atoms with momentum $p/2\hbar k_L = 2 m \pi / \bar{k}$. Equation (13) indicates that the effective stochasticity parameter experienced by an atom falls off with increasing magnitude of the atom's momentum. The details of the falloff are governed by the actual pulse profile. In general, the effective stochasticity parameter K_m is given by the Fourier coefficients of the pulse profile, and can be calculated from the experimental pulse train.

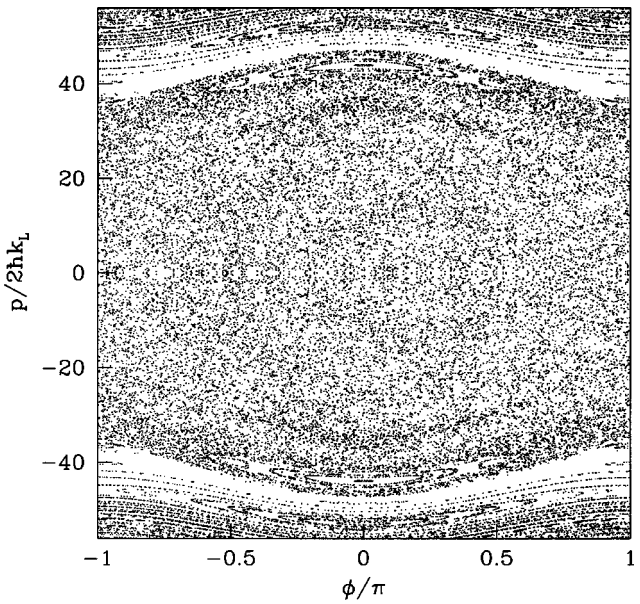

FIG. 3. Poincaré surface of section for the kicked rotor using a train of Gaussian pulses of width $t_p/T = 1/15.8$ (FWHM) to simulate the experimental sequence. The stochasticity parameter in this calculation is $K = 11.6$. The central region of the portrait shows the chaotic motion expected for this value of the stochasticity parameter. Bounded regions due to the finite pulse width are also evident.

The nonzero pulse widths thus lead to a finite number of significant resonances in the classical dynamics. The diffusion resulting from the overlapping resonances is therefore restricted to a band in phase space, limited by an upper momentum boundary and a lower momentum boundary, as shown in Fig. 3. The boundaries to this band of diffusion can be estimated, using Eq. (13), to find the momenta at which the effective stochasticity parameter drops below a value of ~ 4.

The width of the band of diffusion is experimentally controllable. Although the unbounded phase space corresponding to ideal δ-function pulses cannot be practically reached, the width of the band can be made arbitrarily large by decreasing the pulse duration and increasing the well depth. This can be seen as a limiting case of the result in Eq. (13), with K fixed and $\tau_{\mathrm{rms}} \to 0$ (that is, under conditions of large well depth V_o and infinitesimal pulse width t_p). Although Eq. (13) was derived for a Gaussian pulse profile, the widening of the band of diffusion is a general effect that can be achieved by decreasing the pulse duration for any pulse profile.

It is important to note that it is not necessary to have an infinitesimal pulse width to model the δ-kicked rotor. In practice, it is sufficient to choose a pulse width that ensures both that the chaotic band is significantly wider than the range of atomic momenta accessed in the experiment, and that K_m is approximately uniform over this range. These conditions can be achieved by using a sufficiently short pulse duration.

The classical phase portrait shown in Fig. 3 illustrates the bounded region of chaos that arises from the finite pulse duration under typical experimental parameters. The central region of momentum in this phase portrait is in very close correspondence with the δ-kicked rotor model with K

$=11.6$. This stochasticity parameter is well beyond the threshold for global chaos.

Classically, then, the atoms are expected to diffuse in momentum until they reach the momentum boundary that results from the finite pulse width. According to a classical model, the energy of the system $\langle \frac{1}{2}(p/2\hbar k_L)^2 \rangle$ grows linearly in time. In terms of the number of pulses N, this energy is $\langle \frac{1}{2}(p/2\hbar k_L)^2 \rangle = \langle \frac{1}{2}(\rho/\bar{\kappa})^2 \rangle = K^2 N/4\bar{\kappa}^2$.

B. Quantum predictions

The existence of manifestly quantum mechanical behavior in classically chaotic systems has been widely studied and documented over the past several years. The δ-kicked rotor has played an especially important role in these studies because of its well-characterized classical limit and the simple, analytic nature of its time-evolution operator. Of particular interest to us are two phenomena seen in the quantum evolution, dynamical localization [27] and quantum resonances [12].

A quantum analysis of this system starts with the Schrödinger equation [Eq. (4)] for the pulsed modulation of Eq. (10). During the time span of the experiment, this equation can be written as

$$i\bar{\kappa}\frac{\partial \Psi}{\partial \tau} = \left[\frac{-\bar{\kappa}^2}{2}\frac{\partial^2}{\partial \phi^2} + K\cos\phi \sum_{n=-\infty}^{\infty} f(\tau - n) \right] \Psi. \quad (14)$$

The temporal periodicity of the pulses can be exploited, using Floquet's theorem, to describe the dynamics entirely in terms of the Floquet states (the eigenstates of the single-pulse evolution operator) which have been studied extensively in the ideal case of $f(\tau) = \delta(\tau)$ [11]. An analysis of this system by Chirikov, Izrailev, and Shepelyansky [28] shows that this system diffuses classically only for short times during which the discrete nature of the Floquet spectrum is not resolved. An analysis of that system indicates that the Floquet states of Eq. (14) are exponentially localized in momentum. Since these states form a complete basis for the system, the initial condition of an atom in the experiments can be expanded in a basis of Floquet states. Subsequent diffusion is limited to values of momentum covered by those Floquet states that overlap with the initial conditions of the experiment. As seen for the ideal rotor, the energy of the system should grow linearly with the number of kicks N, in agreement with the classical model, until a ''quantum break time'' N^*. After this time, the momentum distribution approaches that of the Floquet states that constituted the initial conditions, and the linear growth of energy is curtailed. This is the phenomenon of dynamical localization. As shown in Ref. [13], an explicit analogy can be made with the phenomenon of Anderson localization by transforming Eq. (14) into the form of the tight-binding model of condensed-matter physics.

The Floquet states are typically localized with an exponential distribution in momentum, $|\Psi(\rho/\bar{\kappa})|^2 \sim \exp(-|\rho/\bar{\kappa}|/\xi)$, characterized by a ''localization length'' ξ. The momentum distribution has a $1/e$ half-width given by $p^*/2\hbar k_L = \rho^*/\bar{\kappa} \equiv \overline{\xi}$, where $\overline{\xi}$ is the average localization length of the Floquet states. A heuristic estimate [28,29] for the localization length in terms of the stochasticity parameter and the quantization scale is $\overline{\xi} = K^2/4\bar{\kappa}^2$.

In our experiments it was the rms momentum that we derived from each measured distribution, since its definition applies as well to the prelocalized Gaussian distributions as to the exponentially localized ones. For an exponential distribution, this quantity is larger than the localization length by a factor of $\sqrt{2}$: $p^*_{\rm rms}/2\hbar k_L = \sqrt{2}K^2/4\bar{\kappa}^2$. According to the heuristic estimate, $\overline{\xi}$ is also a measure of the number of kicks before diffusion is limited by dynamical localization, so for the quantum break time we have $N^* = \overline{\xi} = K^2/4\bar{\kappa}^2$.

An inherent assumption in the derivation of heuristic estimate was the lack of structure in the phase space of the system. Small vestigial islands of stability, however, do persist for values of K greater than 4. This structure introduces in the dynamics a dependence on the location of the initial conditions in phase space, which is usually characterized by fluctuations in the localization length.

It is important to consider the above two estimates of the localization length and the quantum break time when choosing experimental parameters. In order for a localized distribution to be observable, $p^*_{\rm rms}$ must be significantly smaller than the region enclosed by the classical boundary to diffusion. The localized momentum distribution, achieved after the quantum break time, must also be wider than the initial distribution. These two considerations dictate an upper bound of the duration of each kick. Other considerations similarly lead to constraints on the experimental parameters [20,15].

C. Experimental results and analysis

We subjected the cooled and trapped atoms to the periodically pulsed standing wave of Eq. (9), and recorded the resulting momentum distributions as was described in Sec. III. To study the temporal evolution of the atomic sample under the influence of the periodic kicks, these measurements were repeated, starting from identical initial atomic distributions and with the well depth, pulse period, and pulse duration fixed, but with increasing numbers of kicks (N). These successive measurements provided the momentum distributions at different times in the atomic sample's evolution. Such a series of measurements is shown in Fig. 4. Here the pulse had a period of $T = 1.58$ μs, and a FWHM duration of $t_p = 100$ ns. For these conditions, $\bar{\kappa}$ has a value of 2.0. The largest uncertainty in the experimental conditions is in the well depth V_o, which depends on the measurement of the absolute power of the laser beams that make up the standing wave and their spatial profile over the sample of atoms. To within 10%, the well depth for these data had a spatial rms value of $V_o/h = 9.45$ MHz. The pulse profile was nearly square, leading to a stochasticity parameter of $K = 11.6$, the same value as for the phase portrait in Fig. 3.

The distributions clearly evolve from an initial Gaussian at $N = 0$ to an exponentially localized distribution after approximately $N = 8$ kicks. We measured distributions out until $N = 50$, and found no further significant change. The small peak on the right side of this graph is due to nonuniformities in the detection efficiency. As discussed in Sec. III, the relative numbers of atoms with different momenta is measured

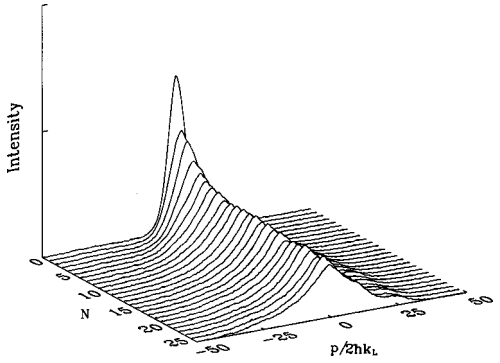

FIG. 4. Experimental time evolution of the momentum distribution from the initial Gaussian until the exponentially localized distribution. N indicates the elapsed number of kicks. The break time is approximately eight kicks. Fringes in the freezing molasses led to small asymmetries in some of the measured momentum distributions, as seen here and in the inset of Fig. 5. The vertical scale is measured in arbitrary units and is linear.

by their fluorescence intensity on a CCD camera. Factors such as spatial variations in the illuminating light and unevenness in the chamber windows between the atomic sample and the CCD camera lead to minor limitations like this on the resolution of the momentum measurements.

The growth of the mean kinetic energy of the atoms as a function of the number of kicks was calculated from the data, and is displayed in Fig. 5. It shows an initial diffusive growth until the quantum break time $N^*=8.4$ kicks, after which dynamical localization is observed [30]. The solid line in this figure represents the predicted classical diffusion; the data follow this prediction until the break time. The dashed line in the same figure is the heuristically calculated energy of the localized distribution. Though not shown here, classical and quantum calculations both agree with the data over the diffusive regime. After the quantum break time, the classical growth would slow slightly due to the falloff in K predicted by Eq. (13) for nonstationary atoms. The observed distribution would lead to a reduction of only 15% in the stochasticity parameter. Thus, the classically predicted energy would continue to increase diffusively. The measured distributions, however, stop growing, as predicted by the quantum analysis.

D. Quantum resonances

Another intrinsically quantum-mechanical effect anticipated by theoretical analyses of the δ-kicked rotor is the phenomenon of quantum resonances, which results from appropriately-chosen values of the kicking period T. Between kicks, the atoms undergo free evolution for a fixed duration. During a free-evolution period, a plane wave with momentum p_o accumulates a quantum phase proportional to its energy, and evolves by a phase factor $\exp[-ip_o^2T/2M\hbar]$ $=\exp[-i(p_o/2\hbar k_L)^2 4\omega_r T]$. During a kick, when the atom is exposed to the optical potential, the initial state only couples to other plane waves with momenta $p_o \pm 2m\hbar k_L$ (with integer m). This restriction to a ladder of momentum states separated by two photon recoils is dictated by the periodicity of the optical potential, as discussed earlier (Sec. II B).

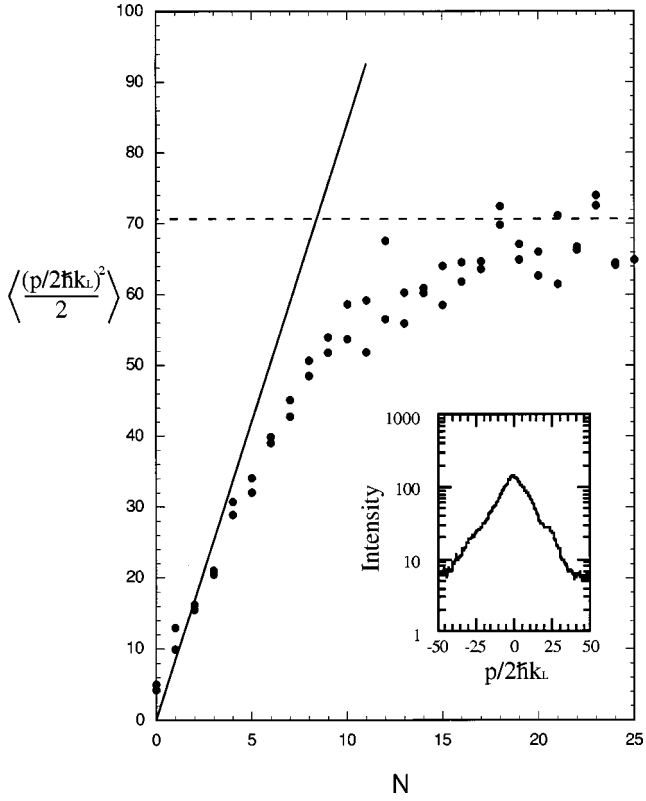

FIG. 5. Energy $\langle (p/2\hbar k_L)^2\rangle/2$ as a function of the number of kicks (N). The solid dots are the experimental results. The solid line shows the linear growth predicted by the classical theory. The dashed line is the saturation value computed from the theoretical localization length ξ. No adjustable parameters were used in determining the theoretical values. The inset shows an experimentally measured exponential distribution, on a logarithmic scale, that is consistent with the theoretical prediction. Exact numerical simulations (not shown) closely match the experimental data.

If the initial momentum p_o is zero or an integer multiple of two photon recoils—an ''integer-momentum state,'' then particular values of the pulse period T lead to phase factors of unity for the free-evolution. This condition, known as a quantum resonance [12], occurs when the pulse period T is chosen so that the free-evolution coefficient $4\omega_r T(=k/2)$ is a multiple of 2π. Quantum resonances have been studied theoretically, and it was shown that at these values of the pulse period, the atoms are not expected to demonstrate localization. Instead, the atoms should show a ballistic motion, in which the energy grows quadratically with time [12]. We have scanned T from 3.3 to 50 μs, and observed quantum resonances when the free-evolution coefficient was chosen to be an integer multiple of π. The even multiples led to a phase factor between kicks of unity; the odd multiples led to a phase factor of -1 (a flipping of sign between each kick), and exhibited similar behavior.

Our experimental results are shown in Fig. 6. Ten quantum resonances were found for T ranging between 5 μs (corresponding to an evolution factor of π) and 50 μs (10π) in steps of 5μs. Under each of these resonance conditions the atomic sample expanded to a saturated final momentum distribution—a behavior qualitatively different from the anticipated ballistic motion. The final distributions were also unlike the dynamically localized distributions discussed ear-

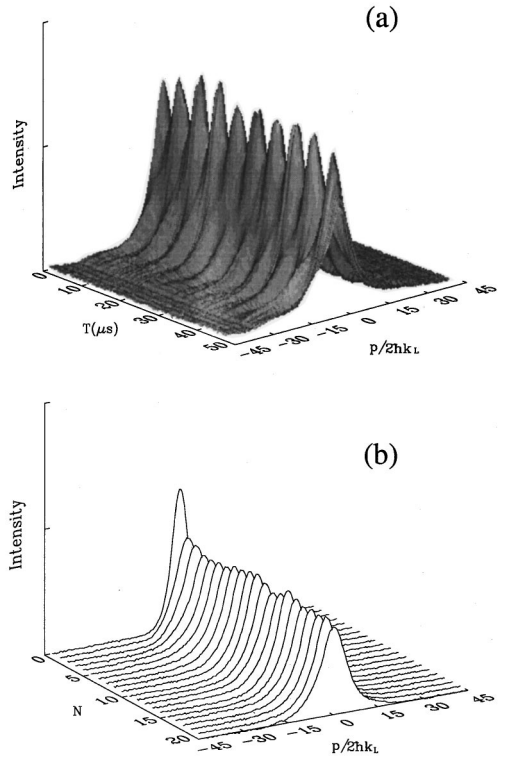

FIG. 6. Experimental observation of quantum resonances: (a) Occurrence as a function of the period (T) of the pulses. The surface plot is constructed from 150 momentum distributions measured, for each T, after $N=25$ kicks. This value of N ensures that the momentum distributions are saturated for the entire range of T shown. On resonance, the profiles are nonexponential and narrower than the localized distributions that appear off resonance. Note that the vertical scale is linear. (b) Time evolution of a particular resonance ($T=10$ μs).

lier, in that they did not exhibit the hallmark exponential profiles. The saturated momentum distributions as a function of T are shown in Fig. 6(a). The narrower, nonexponential profiles are the resonances, between which the exponentially localized profiles are recovered. The time evolution of the distribution at one particular resonance is shown in Fig. 6(b), from which it is apparent that the observed distribution saturates after very few kicks.

Why is the observed behavior so different from the prediction of ballistic motion? The earlier analysis of quantum resonances [12] considered only the evolution of integer-momentum states, so the momenta were restricted to values of $p=2n\hbar k_L$, with integer values of n. (In the dimensionless units, this restriction is $\rho=\bar{k}n$.) This is clearly not the appropriate basis in our experiments, in which the initial sample of atoms was an ensemble distributed continuously in momentum. An appropriate model for our experiments must recognize this continuous distribution.

The following analysis proceeds from a more general consideration of dynamics. The time-evolution operator over one kicking period is $U=\exp(-i(n+\nu)^2\bar{k}/2)\exp(-iK\cos\phi/\bar{k})$, where the momentum (in the dimensionless units) is $\rho=\bar{k}(n+\nu)$ with an integer part n and a quasimomentum $\nu\in[-\frac{1}{2},\frac{1}{2})$. When the pulse period T satisfies the condition for quantum resonances, this relation reduces to $U=\exp(-i\bar{k}n\nu)\exp(-iK\cos\phi/\bar{k})$, where the first term corresponds to a linear kinetic term. (Here a phase that depends only on the quasimomentum has been dropped.) Hence the dynamics are integrable and the evolution of the wave function across the sth kick is given by $\psi_s(\phi)=e^{-iK\cos(\phi-\bar{k}\nu)/\bar{k}}\psi_{s-1}(\phi-\bar{k}\nu)$, where we have used the fact that $\exp(-i\bar{k}n\nu)$ is a space-translation operator.

We can iterate this relation to determine the behavior of a single plane-wave state. Starting from an initial state $\Psi_0(\phi)$ with momentum $\rho_o=\bar{k}(n_o+\nu_o)$, we find that after N kicks, the wave function evolves to

$$\Psi_N(\phi)=\exp\left(-i\frac{K}{\bar{k}}\sum_{l=0}^{N-1}\cos[\phi-(N-l)\bar{k}\nu_o]\right)\times e^{i(n_o+\nu_o)(\phi-N\bar{k}\nu_o)}=\sum_{n=-\infty}^{\infty}a_n e^{i(n+\nu_o)\phi}, \tag{15}$$

with

$$a_n\propto J_{n-n_o}\left(\frac{K}{\bar{k}}\frac{\sin N\beta_o}{\sin\beta_o}\right), \tag{16}$$

and with $\beta_o=\bar{k}\nu_o/2$. Thus the final wave function has components on a ladder of evenly spaced momentum states at $\bar{k}(n+\nu_o)$. The amplitudes a_n have a dependence on the number of elapsed kicks N through the ordinary Bessel functions J_n. Their periodic dependence on N causes recurrences in time that are related to the ''antiresonances'' discussed recently [31] in a different context.

The quantity $|a_n|^2$ obtained from Eq. (16) indicates the distribution in momentum resulting after N kicks from an initial plane wave with momentum ρ_o. Note that in the special case where the initial state is an integer-momentum state ($\nu_o=0$), we recover the expected ballistic motion: the momentum distribution is $|a_n|^2=J^2_{n-n_o}(NK/\bar{k})$, with an energy that grows quadratically with the number of elapsed kicks N. For initial momentum states with $\nu_o\neq 0$, the motion is ballistic for a time $N\ll 1/\beta_o$, after which the wave function is bounded in momentum ρ with a width of $\sim 2K/\sin\beta_o$.

The final step to comparing with the experimentally measured distributions is an ensemble average over the initial momentum distribution of the atomic sample, $F_i(\rho_o)=A\exp[-\bar{k}^2(n_o+\nu_o)^2/2\sigma^2_{\rho o}]$, where $\sigma_{\rho o}$ is the initial width of the distribution. The final momentum distribution of the ensemble after N kicks is then given by

$$F_f(\rho)=A\sum_{n'}\exp[-\bar{k}^2(n'+\nu)^2/2\sigma^2_{\rho o}]J^2_{n-n'}\left(\frac{K}{\bar{k}}\frac{\sin N\beta}{\sin\beta}\right), \tag{17}$$

where n and ν are the integer and fractional parts of the momentum $\rho=\bar{k}(n+\nu)$, and where $\beta=\bar{k}\nu/2$. A comparison of the analytic expression for the momentum distribution with the experimentally measured ones for the first six kicks is shown in Fig. 7. The observed evolution clearly supports

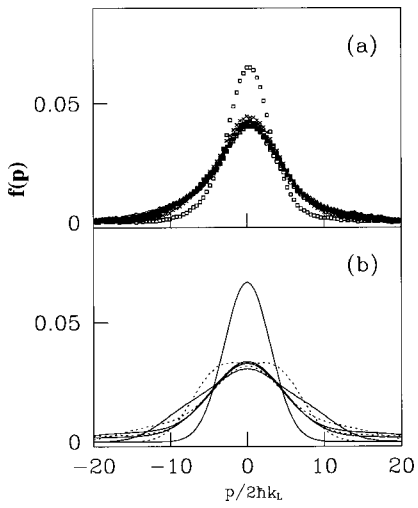

FIG. 7. Evolution of the momentum distribution at a particular resonance ($T=10\ \mu$s) over the first six kicks. The experimental points are shown in panel (a), while the analytic expression derived in the text is used to obtain the curves shown in panel (b). No adjustable parameters were used in this calculation.

the analysis. Estimates of the temporal widths of the quantum resonances, $\propto \overline{\xi}^{-1/2}$, are also readily obtained [32].

Are there signatures of the ballistic motion hidden in the experimental curves? Figure 8 shows numerical simulations of the time evolution for three distinct situations. Figure 8(a) considers the case where the quantum resonance condition is not satisfied. The expected exponentially localized distribution develops beyond the break time. The evolution shown in Fig. 8(b) is at a quantum resonance, and it results in a momentum distribution that is considerably narrower than the localized momentum distribution of Fig. 8(a). As shown above, this is a consequence of the integrable evolution for the noninteger-momentum initial conditions. Figure 8(c) considers a very narrow, near-plane-wave initial condition for which the predicted ballistic motion is recovered. On closer scrutiny, a ridge corresponding to the ballistic evolution of *part of the initial condition* is clearly visible in Fig. 8(b), though the associated signal was below the available resolution of the experiments. This signal would be enhanced in experiments that started with narrower initial momentum distributions.

The observed behavior at the quantum resonances is a consequence of the non-plane-wave initial conditions and, in particular, of the weighted sum of evolutions for all allowed values of the quasimomentum. In fact, this is an important aspect of simulating the conditions of the experiment and must be considered even in the Floquet analysis, an issue we will return to during our quantum analysis of experiments in Sec. V.

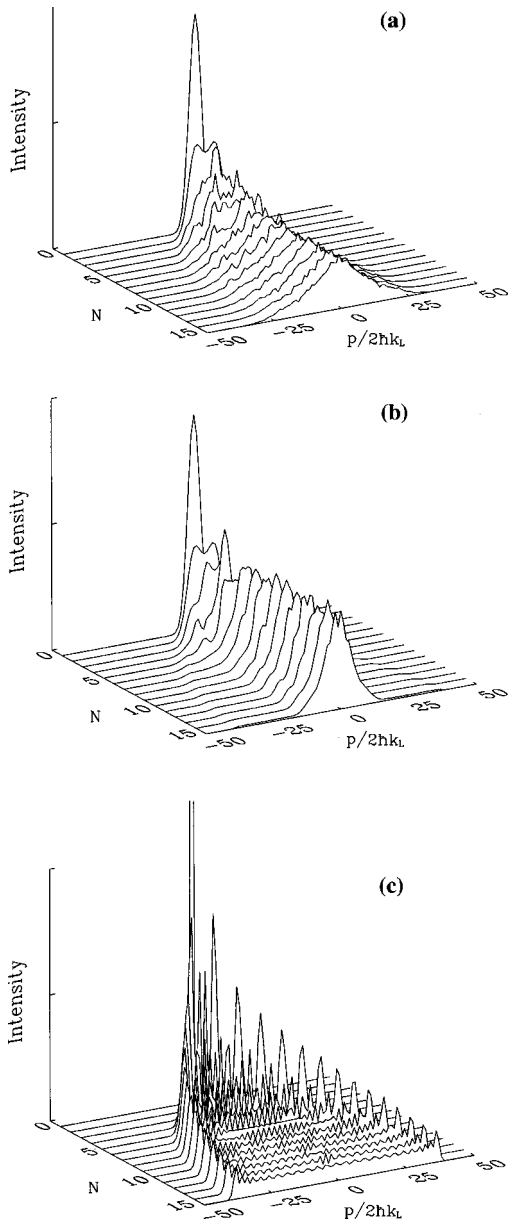

FIG. 8. Quantum simulations of evolution of the momentum distribution (a) away from any quantum resonance, (b) at a quantum resonance for an initial packet with the experimental momentum width, and (c) at resonance but with a narrow initial momentum distribution. See the text for discussion of the ridge seen in panel (b).

V. MODULATED STANDING WAVE

Dynamical localization is not a phenomenon unique to the δ-kicked rotor, but is observable in other systems as well. Following a suggestion by Graham, Schlautmann, and Zoller [33], we carried out experiments in which the interaction potential had a constant amplitude, but in which the phase of the standing wave was modulated. In these experiments, we subjected our atoms to a standing wave of near-resonant light in which the nodal pattern was modulated at a frequency ω_m and with an amplitude ΔL. Once again, a large detuning was used to eliminate the upper level dynamics of the two-level-atom model, leading to an effective Hamiltonian given by Eq. (2), with $F_{\mathrm{amp}}(t)=1$ and $F_{\mathrm{ph}}(t)=2k_L\,\Delta L\sin\omega_m t$:

$$H=\frac{p^2}{2M}+V_o\cos[2k_L(x-\Delta L\sin\omega_m t)]. \tag{18}$$

Although this Hamiltonian may look somewhat different than the δ-kicked rotor, it also displays the phenomenon of dynamical localization. Indeed, our experiments with this modulated standing wave preceded our realization of the

kicked rotor, and provided our first observations of dynamical localization. These experiments are further described in this section.

A. Classical analysis

The resonance structure of the system can be exposed by expanding the Hamiltonian (18) in a discrete Fourier series,

$$H=\frac{p^2}{2M}+V_o\sum_{n=-\infty}^{\infty}J_n(\lambda)\cos 2k_L(x-nv_mt), \qquad (19)$$

where J_n are ordinary Bessel functions, $v_m\equiv\omega_m/2k_L$ is the velocity difference between neighboring resonances, and $\lambda=2k_L\Delta L$ is the modulation index—the amplitude of the phase modulation in radians.

As in the case of the δ-kicked rotor, the resonances are located at regular intervals in momentum. The amplitudes of these resonances, however, depend on a controllable experimental parameter: the modulation index λ. The dependence on λ allows this system to be tuned between regimes where the classical dynamics are integrable (for example, $\lambda=0$) to those in which they are chaotic.

The classical resonances are evenly separated in momentum with central values of $p_n=nMv_m$ and widths of $\Delta p_n=4\sqrt{MV_o|J_n(\lambda)|}$. Therefore, the resonances have substantial widths only for $n\leqslant\lambda$, and for momenta greater than λMv_m the phase space is characterized by essentially free evolution. For certain ranges of λ, these resonances overlap, leading to a band of chaos with boundaries in momentum that are proportional to λ. A sample of atoms starting with initial conditions within this band will remain within it, confined to momenta in the range $\pm M\lambda v_m$. A simple estimate of the atomic momentum after a long time is a uniform distribution within these bounds [33]; such a distribution would have an rms momentum of

$$\frac{p_{\rm rms}}{2\hbar k_L}=\frac{M\lambda v_m}{\sqrt{3}\,2\hbar k_L}=\frac{\lambda}{\sqrt{3}}\frac{\omega_m}{8\omega_r}. \qquad (20)$$

The calculated rms width of the atomic momentum distribution as a function of λ is shown in Fig. 9. Here the modulation frequency was $\omega_m/2\pi=1.3$ MHz and the well depth was $V_o/h=3.1$ MHz. The ergodic estimate of Eq. (20) is denoted by the solid line. For values of $\lambda<3$, this estimate agrees roughly with an integration of the classical Hamilton's equations [34] (shown in the figure) calculated for an interaction time of 20 μs. For larger values of λ, the simulation is lower than the estimate, because in only 20 μs the initial distribution (with $p_{\rm rms}/2\hbar k_L\sim 2.3$) does not have time to diffuse up to the limit represented by the solid line. Except for values of λ close to 7.0 (explained below), the longer-duration classical simulation presented in the figure agrees with the estimate over the entire range of λ shown. The 20-μs classical simulation also shows oscillations in the diffusion rate as a function of λ: peaks in the rms momentum correspond to values of λ leading to large diffusion rates, while dips indicate slow diffusion. The estimated classical boundary of Eq. (20) and the simulations shown in this figure are based on the measured value of V_o, which has an uncertainty of $\pm 10\%$. This uncertainty stems from the measurement of optical power in the interaction beams used in the standing wave.

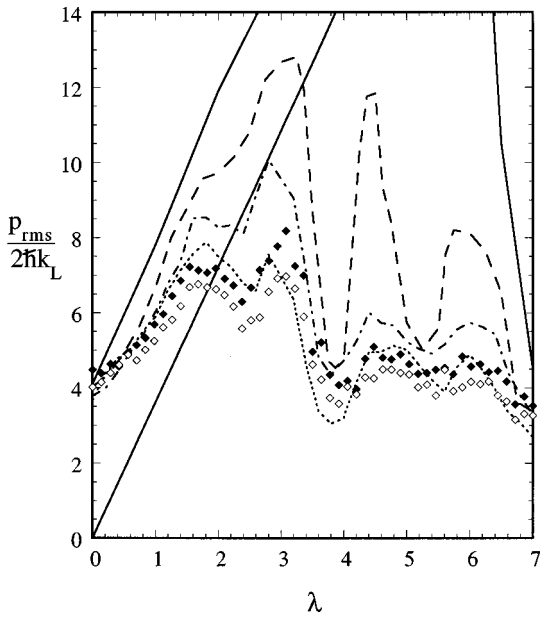

FIG. 9. rms momentum width as a function of the modulation amplitude λ, for $\omega_m/2\pi=1.3$ MHz and $V_o/h=3.1$ MHz. Experimental data are denoted by diamonds. The empty diamonds are for an interaction time of 10 μs, and the solid diamonds are for 20 μs. The straight line denotes the estimated classical boundary from Eq. (20). The four curves indicate numerical simulations. Two integrations of the classical model are shown, one for a simulation time of 20 μs (− − −), and one for the long time limit that shows the maximum diffusion in momentum (———). The observed data lie well below these curves for some values of λ. A 20 μs integration of the Schrödinger equation (. . .) is also presented for comparison with the corresponding experimental data. Also shown is a quantum calculation in which the system's solution was found in terms of its Floquet states (.−.−.).

To understand this variation in diffusion rates, we examine the resonances in Eq. (19). The dependence of the diffusion rate on λ is due to oscillations in $J_n(\lambda)$, which gives the amplitudes of the resonances. The various resonances grow and shrink as the modulation index λ is increased. For certain values of λ, a resonance can be significantly diminished, or even removed in the case where λ is a zero of one of the Bessel functions. As shown in the computer-generated phase portraits of Fig. 10 (top panel), this variation in the amplitudes of the resonances strongly influences the dynamics of the system. In general, the phase spaces are mixed, with islands of stability surrounded by regions of chaos. Atoms from the initial distribution that are contained within an island remain trapped, while those in the chaotic domain can diffuse out to the boundaries. In the case of a diminished resonance, the islands of stability from neighboring resonances might not be destroyed by resonance overlap. This is the case with $\lambda=3.8$, for which $J_1(\lambda)$ has its first zero. The final momentum spread in this case is governed largely by the surviving island due to the resonance at $p_0=0$, and the system is nearly integrable. The stability of this system causes the reduced diffusion shown by the dip in the classical simulation of Fig. 9 at $\lambda=3.8$. Indeed, all of the dips in

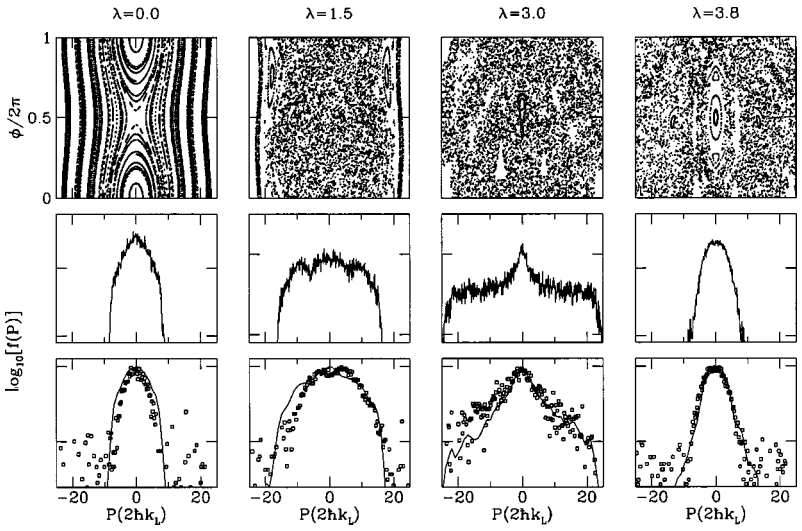

FIG. 10. Poincaré surfaces of section (upper panel), classical momentum distributions (middle panel), and experimentally measured momentum distributions with Floquet theory (bottom panel, theory marked by lines) for runs with parameters similar to those in Fig. 9. The vertical scales for the distributions are logarithmic and are marked in decades.

this simulation occur at values of λ that are near zeros of Bessel functions; the dynamics of the corresponding systems are stabilized by the diminished resonances. This stabilization even affects diffusion in the long-time classical simulation: for values of λ close to 7.0 [the second zero of $J_1(\lambda)$], the initial conditions are trapped in a large island of stability at $p_0=0$. For these values of λ, the diffusion is limited by the width of the island to a region much smaller than that given by the estimated classical boundary.

B. Quantum predictions

We performed a quantum-mechanical calculation of the expected momentum distributions by integrating the Schrödinger equation using the initial squeezed wave packet from Eq. (6). A second quantum simulation was made by finding the Floquet basis states of the system (for particular values of λ) and weighting them by the momentum distribution of the experimental initial conditions. By taking the unit of time to be $1/\omega_m$, we have the dimensionless variables $\tau=\omega_m t$, $\phi=2k_L x$, and $\rho=(2k_L/M\omega_m)p$. We expand the eigenstates of our Hamiltonian in a two-dimensional Floquet state basis, $\{\psi(\phi,\tau)=e^{i\nu\phi}e^{-i\epsilon\tau}u(\phi,\tau)\}$. Here $u(\phi,\tau)$ reflects the periodic structure of the Hamiltonian; that is, $u(\phi+2\pi,\tau)=u(\phi,\tau+2\pi)=u(\phi,\tau)$. ν is the quasimomentum, and ϵ is the quasienergy of a basis state. Expanding $u(\phi,\tau)$ in a Fourier series, in both the space and time variables, allows us to write the basis states in the form $\psi_\epsilon(\phi,\tau)=\Sigma_{mn}\psi^\epsilon_{mn}e^{i(n+\nu)\phi}e^{-i(m+\epsilon)\tau}$. The Schrödinger equation in this representation is then $\epsilon\psi^\epsilon_{mn}=(-m+(\bar{\kappa}/2)(n+\nu)^2)\psi^\epsilon_{mn}-(k/2\bar{\kappa})\Sigma_{l=-\infty}^{\infty}J_l(\lambda)(\psi^\epsilon_{m-l,n-1}+\psi^\epsilon_{m+l,n+1})$, where $k=\bar{\kappa}V_o/\hbar\omega_m$ and $\bar{\kappa}=8\omega_r/\omega_m$.

For each ν, the set of quasienergies and the corresponding basis states are obtained by numerically solving this Schrödinger equation. To make contact with the experiment, we needed to use appropriate initial conditions in the numerical simulations. As described earlier, the initial condition of the atomic sample had a distribution characterized by its width in space ($\sigma_{xo}\sim 0.15$ mm) and momentum ($\sigma_{po}\sim 4.6\hbar k_L$). The sample was therefore an ensemble of atomic states with a spatial extent σ_{xo} wide in comparison to the length scale $\lambda_L/2$ of the periodic potential. Because there was thus no information about the position of the initial states up to a very large length scale, we modeled the initial sample of atoms as a statistical ensemble of momentum eigenstates. The distribution was taken to be a Gaussian in momentum p according to the experimentally measured value of σ_{po}. For each momentum state, we made an expansion in terms of the Floquet states in order to analyze their time evolution. The final momentum distribution was then averaged over the evolution time to determine a distribution $P(p,p_o)$, where p_o is the initial momentum. The final ensemble momentum distribution was found by integrating $P(p,p_o)$ against the initial distribution of p_o.

rms momentum calculations from the two quantum simulations are shown along with the classical calculations in Fig. 9. Momentum distributions calculated from the Floquet analysis are also shown in the lower panel of Fig. 10. For some regimes of well depth and modulation frequency, the quantum simulations closely match the classical simulations. As discussed below, however, the quantum simulations predict exponential distributions with significantly smaller widths in the regimes where the classical dynamics are largely chaotic.

C. Experimental results and analysis

Along with the classical and quantum simulations, Fig. 9 shows our experimental data points (diamonds) for interaction times of 10 and 20 μs [34,35]. The 20-μs data match the classical simulations well for small values of λ and for values of λ that are close to zeros of Bessel functions. For other values of λ, however, the experimentally measured distributions are much narrower than those predicted classically. As was the case in the kicked rotor experiments, the reason for this reduction in the width of the observed momentum distributions is dynamical localization.

In Fig. 9 the empty and solid diamonds are experimental data for the two interaction times; the proximity of the two sets of data points shows that these results are close to saturation for the range of λ shown. At $\lambda=0$ the system is integrable, and momentum is trivially localized. As λ is increased the phase space becomes chaotic, but growth is limited by the estimated classical boundary. Our measured momentum distributions (in Fig. 10, bottom panel) are char-

acteristically ''boxlike'' in this regime ($0 \leqslant \lambda \leqslant 2$). This observation is consistent with the picture of a uniform diffusion limited by the boundaries in momentum.

As λ is increased beyond a critical value, the rms width of the observed momentum distributions exhibits the predicted oscillations as a function of λ. For certain ranges of the modulation index λ, the observed rms widths deviate substantially from the classical prediction. These ranges correspond to conditions of large diffusion rates—at the peaks in rms width of the classical prediction. For these values of λ the classical phase space is predominately chaotic. An example of the resulting dynamics is shown in Fig. 10 for $\lambda = 3.0$. The classically predicted distribution (middle panel) is roughly uniform, but the experimentally observed distribution is exponentially localized by dynamical localization; hence the rms value is reduced.

As λ is increased further, the oscillations in the resonance amplitudes lead to phase portraits with large islands of stability, as in the case of $\lambda = 3.8$. For these values of λ the experimental initial conditions lie in a predominantly stable region in the classical phase space, and the measured momentum is close to the classical prediction.

As can be seen from Figs. 9 and 10, experimental results for both the rms momentum as well as the momentum distributions agreed very well with the quantum analyses. To simplify the Floquet analysis, the small spread in K proportional to laser intensity variations across the ensemble of atoms was approximated by the use of a rms value of K. The rms momentum spread from the Floquet analysis in Fig. 9 (dot-dashed line) and the momentum distributions in Fig. 10 (bottom panel) show good agreement with the experiment over the entire range of λ.

The Floquet analysis once again illustrates the need to consider all values of the quasimomenta ν when analyzing the experimental results. As demonstrated recently [36], failure to do so can lead to spurious inferences [37,38]. Further, the agreement between the plane-wave Floquet analysis, a distribution of minimum-uncertainty states [18] and the results using a squeezed wave packet supports our arguments in Sec. II C and validates the squeezed-wave-packet approach.

VI. SUMMARY

This work establishes an experimental testing ground for quantum chaos, in which it should be possible to study many aspects of this field. These experiments introduce a method of studying one-dimensional quantum systems with virtually ideal spatial periodicity and no noise. The experiments allow direct comparisons to theoretical predictions with no adjustable parameters, and direct control over all experimental parameters.

Some topics for future study include noise-induced delocalization [17,39–41] and localization in two and three dimensions [11]. Using recently developed techniques of atom cooling and manipulation, it should be possible to prepare the atoms in a localized region of phase space. This state preparation technique would enable a detailed study of quantum transport in mixed phase space. Other interesting topics to study would be tunneling from islands of stability, chaos-assisted tunneling, and quantum scars [42].

[1] *Irregular Atomic Systems and Quantum Chaos*, edited by J. C. Gay (Gordon and Breach, New York, 1992).

[2] R. V. Jensen, Nature (London) **355**, 311 (1992).

[3] H. Friedrich and D. Wintgen, Phys. Rep. **183**, 37 (1989); D. Delande, in *Chaos and Quantum Physics*, edited by M.-J. Giannoni, A. Voros, and J. Zinn-Justin (Elsevier, London, 1991).

[4] P. M. Koch and K. A. H. van Leeuwen, Phys. Rep. **255**, 289 (1995).

[5] G. S. Ezra, K. Richter, G. Tanner, and D. Wintgen, J. Phys. B **24**, L413 (1991).

[6] See, for example, contributions in Physica D **83** (1995).

[7] See, for example, *Quantum Chaos: Between Order and Disorder: A Selection of Papers*, edited by G. Casati and B. V. Chirikov (Cambridge University Press, New York, 1995).

[8] Laser cooling and trapping was reviewed by Steven Chu in Science **253**, 861 (1991).

[9] C. S. Adams, M. Sigel, and J. Mlynek, Phys. Rep. **240**, 145 (1994).

[10] This work was reviewed by Graham P. Collins, Phys. Today **48**(6), 18 (1995).

[11] Giulio Casati, Italo Guarneri, and D. L. Shepelyansky, Phys. Rev. Lett. **62**, 345 (1989).

[12] F. M. Izrailev and D. L. Shepelyansky, Dokl. Akad. Nauk (SSSR) **248-249**, 1103 (1979) [Sov. Phys. Dokl. **24**, 996 (1979)]; Theor. Math. Phys. **43**, 553 (1980).

[13] S. Fishman, D. R. Grempel, and R. E. Prange, Phys. Rev. Lett. **49**, 509 (1982); D. R. Grempel, R. E. Prange, and S. Fishman, Phys. Rev. A **29**, 1639 (1984); R. E. Prange, D. R. Grempel, and S. Fishman, in *Proceedings of the Como Conference on Quantum Chaos*, edited by G. Casati (Plenum Press, New York, 1984), p. 205.

[14] P. W. Anderson, Phys. Rev. **109**, 1492 (1958).

[15] Cyrus F. Bharucha, Ph.D. dissertation, University of Texas at Austin, 1997 (unpublished).

[16] Kirk W. Madison, Ph.D. dissertation, University of Texas at Austin, 1998 (unpublished).

[17] S. Fishman and D. L. Shepelyansky, Europhys. Lett. **16**, 643 (1991).

[18] P. J. Bardroff, I. Bialynicki-Birula, D. S. Krähmer, G. Kurizki, E. Mayr, P. Stifter, and W. P. Schleich, Phys. Rev. Lett. **74**, 3959 (1995).

[19] S. Habib, H. Mabuchi, R. D. Ryne, K. Shizume, and B. Sudaram (unpublished).

[20] John C. Robinson, Ph.D. dissertation, University of Texas at Austin, 1995 (unpublished).

[21] E. Raab, M. Prentiss, A. Cable, S. Chu, and D. E. Pritchard, Phys. Rev. Lett. **59**, 2631 (1987).

[22] B. V. Chirikov, Phys. Rep. **52**, 265 (1979).

[23] L. E. Reichl, *The Transition to Chaos in Conservative Classical Systems: Quantum Manifestations* (Springer-Verlag, Berlin, 1992).

[24] R. Blümel, S. Fishman, and U. Smilansky, J. Chem. Phys. **84**, 2604 (1986).

[25] J. B. Taylor, Phys. Rev. Lett. **33**, 1139 (1974).

[26] A. L. Lichtenberg and M. A. Lieberman, *Regular and Chaotic Dynamics* (Springer-Verlag, Berlin, 1991).
[27] G. Casati, B. V. Chirikov, J. Ford, and F. M. Izrailev, in *Stochastic Behavior in Classical and Quantum Hamiltonian Systems*, edited by G. Casati and J. Ford, Lecture Notes in Physics Vol. 93 (Springer, Berlin, 1979), p. 334.
[28] B. Chirikov, F. M. Izrailev, and D. L. Shepelyansky, Sov. Sci. Rev., Sect. C **2**, 209 (1981).
[29] D. L. Shepelyansky, Phys. Rev. Lett. **56**, 677 (1986); Physica D **28**, 103 (1987).
[30] F. L. Moore, J. C. Robinson, C. F. Bharucha, Bala Sundaram, and M. G. Raizen, Phys. Rev. Lett. **75**, 4598 (1995).
[31] I. Dana, E. Eisenberg, and N. Shnerb, Phys. Rev. Lett. **74**, 686 (1995).
[32] Q. Niu and Bala Sundaram (unpublished).
[33] R. Graham, M. Schlautmann, and P. Zoller, Phys. Rev. A **45**, R19 (1992).
[34] J. C. Robinson, C. Bharucha, F. L. Moore, R. Jahnke, G. A. Georgakis, Q. Niu, M. G. Raizen, and Bala Sundaram, Phys. Rev. Lett. **74**, 3963 (1995).
[35] F. L. Moore, J. C. Robinson, C. Bharucha, P. E. Williams, and M. G. Raizen, Phys. Rev. Lett. **73**, 2974 (1994).
[36] Miroslaw Latka and Bruce J. West, Phys. Rev. Lett. **75**, 4202 (1995).
[37] M. G. Raizen, Bala Sundaram, and Qian Niu, Phys. Rev. Lett. **78**, 1194 (1997).
[38] S. Meneghini, P. J. Bardroff, E. Mayr, and W. P. Schleich, Phys. Rev. Lett. **78**, 1195 (1997).
[39] T. Dittrich and R. Graham, Europhys. Lett. **4**, 263 (1987).
[40] B. G. Klappauf, W. H. Oskay, D. A. Steck, and M. G. Raizen, Phys. Rev. Lett. **81**, 1203 (1998).
[41] B. G. Klappauf, W. H. Oskay, D. A. Steck, and M. G. Raizen, Phys. Rev. Lett. **81**, 4044 (1998).
[42] E. J. Heller and S. Tomsovic, Phys. Today **46**(7), 38 (1993).